The Path of Gallium from Chemical Bath into ZnO Nanowires: Mechanisms of Formation and Incorporation

Pierre Gaffuri, Estelle Appert, Odette Chaix-Pluchery, Laetitia Rapenne, M. Salaün, Vincent Consonni

The Path of Gallium from Chemical Bath into ZnO Nanowires: Mechanisms of Formation and Incorporation

Pierre Gaffuri,[†,‡] Estelle Appert,[†] Odette Chaix-Pluchery,[†] Laetitia Rapenne,[†] Mathieu Salaün,[‡] and Vincent Consonni.[°,†]

[†] Univ. Grenoble Alpes, CNRS, Grenoble INP*, LMGP, 38000 Grenoble, France

[‡] Univ. Grenoble Alpes, CNRS, Grenoble INP*, Institut Néel, 38000 Grenoble, France

*Institute of Engineering Univ. Grenoble Alpes

CORRESPONDING AUTHOR FOOTNOTE:

°E-mail: vincent.consonni@grenoble-inp.fr

ABSTRACT

ZnO nanowires grown by chemical bath deposition (CBD) are of high interest, but their doping with extrinsic elements including gallium in aqueous solution is still challenging despite its primary importance for transparent electrodes and electronics, as well as mid-infrared plasmonics. We elucidate the formation mechanisms of ZnO nanowires by CBD using zinc nitrate and hexamethylenetetramine as standard chemical precursors, as well as gallium nitrate and ammonia as chemical additives. A complete growth diagram, revealing the effects of both the relative concentration of gallium nitrate and pH, is gained by combining a thorough experimental approach with thermodynamic computations yielding theoretical solubility plots as well as Zn(II) and Ga(III) species. The role of $Ga(OH)_4^-$ complexes is specifically shown as capping agents on the *m*-plane sidewalls of ZnO nanowires, enhancing their development and hence decreasing their aspect ratio. Additionally, the gallium incorporation into ZnO nanowires is investigated in details by chemical analyses and Raman scattering. They show the predominant formation of gallium substituting for zinc atoms (Ga_{Zn}) in as-grown ZnO nanowires and their partial conversion into Ga_{Zn}-V_{Zn} complexes after post-deposition annealing under oxygen atmosphere. The conversion is further related to a significant relaxation of the strain level in

ZnO nanowires. These findings reporting the physico-chemical processes at work during the formation of ZnO nanowires and the related gallium incorporation mechanisms offer a general strategy for their extrinsic doping and open the way for carefully controlling their physical properties as required for nanoscale engineering devices.

INTRODUCTION

As a low-cost, low-temperature, and easily implemented process, chemical bath deposition (CBD) has received, over the last fifteen years, an overwhelming interest to produce spontaneously-grown vertically aligned ZnO nanowires (NWs) with a controlled structural morphology over a large number of substrates.[1] Its additional combination with advanced lithography techniques has further shown an efficient way to form well-ordered ZnO NWs with a great structural uniformity on pre-patterned nucleation surfaces using selective area growth.[2,3] If the structural morphology of ZnO NWs is of high significance for enhancing the performances of the related nanoscale engineering devices, their extrinsic doping by using additional elements substituting for zinc or oxygen sites during CBD is crucial as well to carefully control their electronic, optical, and electrical properties (i.e. electron density, mobility, …). However, it has not been addressed in details yet despite its primary importance on the performances of the nanoscale engineering devices.

Joo *et al.* added ancillary metal sulfates forming ion complexes in the chemical bath, namely A-type (*e.g.* Cd, Cu, Mg, Ca) and B-type ions (*e.g.* Al, In, Ga) to favor attractive electrostatic interactions with the polar *c*-plane top facet and nonpolar *m*-plane sidewalls at the pH of 11, respectively.[4] The aspect ratio of ZnO NWs was accordingly varied in the broad range of 0.1-100 in that way, but a possible incorporation and doping was excluded owing to the use of a low growth temperature. In the framework of that approach, Verrier *et al.* subsequently showed that the adsorption of $Al(OH)_4^-$ complexes as capping agents on the sidewalls of ZnO NWs results in the further incorporation of Al in their center following a thermal annealing from the low temperature of 200 °C.[5] The Al incorporation process was additionally found to be strongly related to the pH and a comprehensive diagram was reported as an efficient strategy to dope ZnO NWs by CBD.[6]

Alternatively to Al, the Ga incorporation into ZnO NWs and its related doping have emerged as highly promising for a variety of nanoscale engineering devices, especially in the fields of transparent electrodes for photovoltaics, transparent electronics, and mid-infrared plasmonics. In particular, the doping efficiency of Ga into ZnO is much larger than its Al counterpart because the ionic radius of Ga^{3+} is closer to the Zn^{2+} radius than the Al^{3+} radius, opening the way for higher doping levels in ZnO.[7] The

evolution of the structural morphology of ZnO NWs grown by CBD, when $Ga(NO_3)_3$ is used as a chemical additive in the chemical bath, has been reported.[8–18] However, some of the findings are in apparent discrepancy because the critical parameters including the pH and $Ga(NO_3)_3$ concentration in the chemical bath as well as the Ga content into the ZnO NWs have not systematically been measured, nor varied on a broad range, nor combined with theoretical thermodynamic simulations. Recently, Lim *et al.* and Park *et al.* showed a decrease in the *c*-lattice parameter of ZnO NWs and an increase in their mean diameter when the $Ga(NO_3)_3$ concentration in the chemical bath was increased.[14,15] Conversely, Li *et al.* observed no effect on the *c*-lattice parameter, and a decrease in the mean diameter of ZnO NWs.[16] The pH has not been reported in those three papers. In contrast, Pineda-Hernández *et al.* and Saravanakumar *et al.* investigated the spontaneous growth of ZnO nanostructures by CBD at a given pH of 12 following the addition of NaOH.[11,17] They showed the shift of Raman lines in the spectra of wurtzite ZnO, as well as the occurrence of Ga related additional modes (AM_{Ga}). Those observations have been achieved on ZnO NWs homogeneously nucleated in the chemical bath, instead of vertically aligned ZnO NWs heterogeneously nucleated onto a substrate covered with a ZnO seed layer. In these papers, the regular additional modes (AMs) commonly observed in Ga-doped ZnO thin films[19] have surprisingly not been reported either.

In this article, the $[Ga(NO_3)_3]$ / $[Zn(NO_3)_2]$ ratio and the pH of the solution are systematically varied over a broad range of 0-10 % and 7.1-11.3, respectively, to elucidate their effects on the structural morphology of ZnO NWs. Speciation diagrams and theoretical solubility plots of Zn(II) and Ga(III) species are calculated to account for the experimental data. Moreover, the Ga incorporation into ZnO NWs is thoroughly investigated by energy-dispersive x-ray spectroscopy (EDS) analyses and temperature-dependent Raman scattering. The findings result in a comprehensive diagram reporting the physico-chemical processes in aqueous solution and the basic mechanisms during post-deposition annealing to simultaneously engineer the shape and dimensions of ZnO NWs while incorporating a given Ga content in their center.

METHODS

Deposition techniques. ZnO NW arrays were grown on *c*-axis oriented polycrystalline ZnO seed layers deposited on a (001) silicon wafer, using a two-step chemical synthesis process. The polycrystalline ZnO seed layers were deposited by the sol-gel process using dip coating. To form the sol, an equimolar mix of 375 mM of both zinc acetate dihydrate ($Zn(CH_3COO)_2.2H_2O$, Emsure ACS) and monoethanolamine (MEA, Sigma-Aldrich) was added in pure ethanol. The solution was heated and stirred at 60 °C for 12 h, and then at room temperature for 12 h more. To form the xerogel film, the silicon wafer was dipped in the solution and withdrew at the speed of 3.3 mm/s in ambient atmosphere with a hygrometry smaller than 15 %. The xerogel film was annealed in air on a hot plate kept at 300 °C for 1 h to evaporate solvent and organic residues, and on another hot plate kept at 500 °C for 3 h to achieve its crystallization.

The growth of vertically aligned ZnO NWs was performed by CBD. The ZnO seed layer-coated silicon wafer was immersed face down in a sealed beaker containing an equimolar mix of 30 mM of zinc nitrate hexahydrate ($Zn(NO_3)_2.6H_2O$, Sigma-Aldrich) and HMTA ($C_6H_{12}N_4$, Sigma-Aldrich) in deionized water. The pH of the solution prior to heating (denoted here as pH_0) was tuned by the addition of ammonia (NH_3, VWR Chemicals). In order to extrinsically control the n-type doping of ZnO NWs, gallium nitrate hydrate ($Ga(NO_3)_3.xH_2O$, Sigma-Aldrich) was used as a chemical additive with a concentration in the range of 0 to 3 mM. The sealed beaker containing the solution was placed in a regular oven heated at 85 °C for 3 h. Both the pH and temperature of the solution were monitored an *in situ* manner to follow their variation as CBD proceeds. The different CBD conditions used are summarized in Table 1. The first series of six samples consisted in achieving the CBD of ZnO NWs at a given $[Ga(NO_3)_3]$ / $[Zn(NO_3)_2]$ ratio of 5 % while varying the pH_0 from 7.1 to 11.3 by the addition of NH_3 with a concentration ranging from 11 to 1167 mM, respectively. The second series of six samples consisted in performing the CBD of ZnO NWs at a given pH_0 of 10.9 using a NH_3 concentration of 584 mM while varying the $[Ga(NO_3)_3]$ / $[Zn(NO_3)_2]$ ratio from 0 to 10 %.

Table 1. Conditions used during the CBD of ZnO NWs for the two series of six samples

$\frac{[Ga(NO_3)_3]}{[Zn(NO_3)_2]}$	pH_0	$[NH_3]$ (mM)
5 %	7.1	11
5 %	10.4	350
5 %	10.7	467
5 %	10.9	584
5 %	11	730
5 %	11.3	1167
0 %	10.9	584
0.5 %	10.9	584
1 %	10.9	584
2.5 %	10.9	584
5 %	10.9	584
10 %	10.9	584

Characterization techniques. The pH and temperature of the solution as CBD proceeds were monitored in an *in situ* manner using an InLab Versatile Pro pH electrode from Mettler Toledo. The morphology and structural properties of ZnO NWs were measured by top-view and cross-sectional view FESEM images using a FEI Quanta 250 field-emission-gun scanning electron microscope. X-ray diffraction patterns were collected with a Bruker D8 Advance diffractometer using Cu $K_{\alpha 1}$ radiation according to the Bragg−Brentano configuration. The Ga incorporation into ZnO NW arrays was investigated by EDS analyses and temperature-dependent Raman scattering measurements. FESEM-EDS spectra of ZnO NW arrays were recorded using a Bruker x-ray detector incorporated in the FEI Quanta 250 field-emission-gun scanning electron microscope operating at 20 kV. STEM specimens were prepared by scratching the surface of ZnO NW arrays using a diamond tip and spread on a copper (Cu) grid. STEM-EDS spectra and maps of single ZnO NWs were collected with a JEOL SDD Centurio detector having a large solid angle of up to 0.98 steradians incorporated in the JEOL 2100F field-emission-gun scanning electron microscope operating at 200 kV and having a 0.2 nm resolution in the scanning mode. Raman scattering spectra were recorded using a Horiba/Jobin Yvon Labram spectrometer equipped with a liquid-nitrogen-cooled CCD detector. The 488 nm excitation line of an Ar^+ laser was used with a power on the sample surface lower than 3 mW. The laser beam was focused to a spot size of 1 μm^2 using a 50 times long working distance objective. The spectra were calibrated in wavenumber at room temperature by using a silicon reference sample and considering that the theoretical position of the silicon Raman line is set to 520.7 cm^{-1}. *In situ* post-deposition annealing was

performed under an oxygen atmosphere from room temperature to 500 °C. The temperature was controlled using a commercial Linkam heating stage (THMS600) placed under the Raman microscope.

Thermodynamic Computations. Thermodynamic simulations were performed by using Visual MINTEQ software to determine the speciation diagrams of Zn (II) and Ga(III) species as well as the theoretical solubility plots of ZnO at 85 °C for each growth condition (*i.e.*, with varying NH_3, $Zn(NO_3)_2$, and $Ga(NO_3)_3$ concentrations). The two single metallic cations in aqueous solution (Zn^{2+} and Ga^{3+} ions) denoted as M^{x+} are capable of forming amine and/or hydroxide complexes with the two possible ligands (NH_3 and HO^-) denoted as L, according to the general reactions: $nM^{x+} + iL \leftrightarrow M_nL_i^{x+}$, where $M_nL_i^{x+}$ is the complex considered, i is the coordination number, and x is the cation charge. The related stability constants β_i^L associated to each reaction are given by: $\beta_i^L = \frac{[M_nL_i^{nx+}]}{[M^{x+}]^n[L]^i}$. These constants were taken at 25 °C from NIST for Zn(II) and Ga(III) species. The constants at 85 °C were deduced from Van't Hoff relation. To calculate the theoretical solubility plots for each growth condition, ZnO(s) and the different phases of $Zn(OH)_2$(s) were taken into account.

RESULTS AND DISCUSSION

Effects of the pH_0 of the solution and of the $Ga(NO_3)_3$ Relative Concentration on the Growth Mechanisms of ZnO Nanowires

Structural morphology of ZnO nanowires - ZnO NWs were grown on *c*-axis oriented polycrystalline ZnO seed layers with the same structural morphology. Their nucleation occurs on semipolar and polar *c*-plane ZnO nanoparticles composing the seed layer,[20,21] which additionally transfer their O- or Zn-polarity.[22] The morphology of ZnO NWs grown by CBD at a given $[Ga(NO_3)_3]$ / $[Zn(NO_3)_2]$ ratio of 5 % while varying the pH_0 from 7.1 to 11.3 by the addition of NH_3 is presented in **Figure 1a** using FESEM imaging. The morphology of ZnO NWs grown by CBD at a given pH_0 of 10.9 while tuning the $[Ga(NO_3)_3]$ / $[Zn(NO_3)_2]$ ratio in the range of 0-10 % is presented in **Figure 1b**. The length, diameter, and apparent number density of ZnO NWs were systematically measured over a large number of nano-objects from such FESEM images, while their aspect ratio and deposited volume were deduced from

these structural characteristics. The morphological properties of ZnO NWs as a function of the pH_0 and of the $[Ga(NO_3)_3]$ / $[Zn(NO_3)_2]$ ratio are summarized in **Figure 2a,b**, respectively.

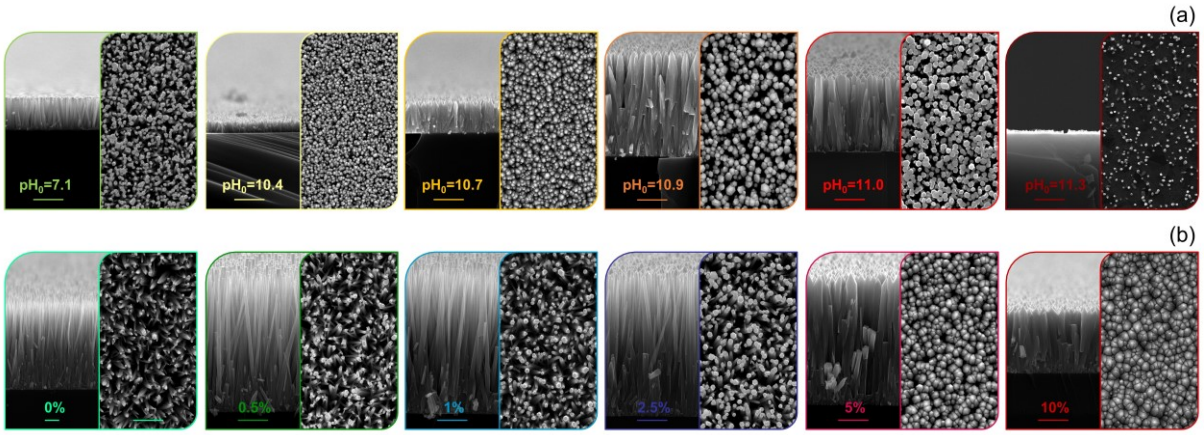

Figure 1. (a) Cross-sectional view and top-view FESEM images of ZnO NWs grown by CBD with pH_0 values in the range of 7.1-11.3 and for a given $[Ga(NO_3)_3]$ / $[Zn(NO_3)_2]$ ratio of 5 %. (b) Cross-sectional view and top-view FESEM images of ZnO NWs grown by CBD with $[Ga(NO_3)_3]$ / $[Zn(NO_3)_2]$ ratio values in the range of 0-10 % and for a given pH_0 of 10.9. The scale bar is 1 µm.

ZnO NWs grown at a pH_0 of 7.1 have a very similar morphology as ZnO NWs grown by CBD using the standard chemical precursors (*i.e.*, $Zn(NO_3)_2$ and HMTA) with no $Ga(NO_3)_3$.[23] They have a flat hexagonal tip and exhibit an aspect ratio of 12 ± 3 with an apparent number density around 60 μm^{-2}. In the pH_0 intermediate range of 7.1-10.4, negligible heterogeneous growth proceeds, because the homogeneous growth in aqueous solution is strongly predominant. In the pH_0 range of 10.4-11.0, all ZnO NWs have a pencil-like shape at their tip. From a pH_0 of 10.4 to 10.9, the length and diameter of ZnO NWs strongly increase from 0.4 ± 0.15 µm to 3.1 ± 0.3 µm and from 90 ± 14 nm to 184 ± 13 nm, respectively. In contrast, their apparent number density strongly decreases from 170 ± 17 to 35 ± 4 μm^{-2}, which is accounted for by highly pronounced coalescence effects. Correlatively, the deposited volume of ZnO NWs jumps from 0.4 ± 0.2 to 2.9 ± 0.7 μm^3. As the pH_0 is further increased from 10.9 to 11.3, all the morphological characteristics of ZnO NWs, including their length, diameter, and deposited volume, fall. At a maximum pH_0 of 11.3, the deposited volume is very low and ZnO NWs are very short, exhibiting a very small aspect ratio.

ZnO NWs grown in the $[Ga(NO_3)_3]$ / $[Zn(NO_3)_2]$ ratio range of 0-2.5 % have a flat hexagonal tip. In contrast, they exhibit a pencil-like shape on their tip when grown in the $[Ga(NO_3)_3]$ / $[Zn(NO_3)_2]$ ratio

range of 2.5-10 %, as shown in **Figure S1**. Also, ZnO NWs are strongly coalesced into a columnar film when grown at the $[Ga(NO_3)_3]$ / $[Zn(NO_3)_2]$ ratio of 10 %. The length of ZnO NWs strongly decreases from 5.3 ± 0.6 to 1.8 ± 0.3 µm, while their diameter increases from 77 ± 6 to 170 ± 30 nm in the $[Ga(NO_3)_3]$ / $[Zn(NO_3)_2]$ ratio range of 0-10 %. Correlatively, their aspect ratio decreases from 69 ± 20 to 10 ± 4. The apparent number density of ZnO NWs first increases in the $[Ga(NO_3)_3]$ / $[Zn(NO_3)_2]$ ratio range of 0-1 % from 40 ± 4 to 52 ± 5 μm^{-2}, and then decreases to reach a plateau around 40 ± 5 μm^{-2}. In contrast, the deposited volume increases from 1.0 ± 0.3 to 3.1 ± 1.5 μm^3 as the $[Ga(NO_3)_3]$ / $[Zn(NO_3)_2]$ ratio is increased from 0 to 5 %, and eventually decreases to 1.7 ± 0.8 μm^3 at the $[Ga(NO_3)_3]$ / $[Zn(NO_3)_2]$ ratio of 10 %.

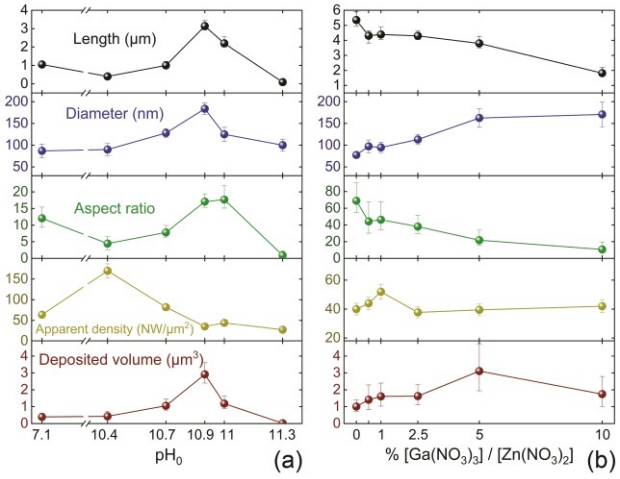

Figure 2. (a) Evolutions of the length, diameter, aspect ratio, apparent number density, and deposited volume of ZnO NWs as a function of the pH_0 and for a given $[Ga(NO_3)_3]$ / $[Zn(NO_3)_2]$ ratio of 5 %. (b) Evolutions of the length, diameter, aspect ratio, apparent number density, and deposited volume of ZnO NWs as a function of the $[Ga(NO_3)_3]$ / $[Zn(NO_3)_2]$ ratio and for a given pH_0 of 10.9.

Effects of the supersaturation in the chemical bath - In order to deeply understand the evolution of the morphological properties of ZnO NWs as a function of the pH_0 and of the $[Ga(NO_3)_3]$ / $[Zn(NO_3)_2]$ ratio, *in situ* pH measurements as CBD proceeds are presented in **Figure 3**. At the beginning of the growth, a sharp drop in the pH is revealed, regardless of the pH_0 values and for all the $[Ga(NO_3)_3]$ / $[Zn(NO_3)_2]$ ratios. This is mainly attributed to the heating of the solution up to 85 °C as well as to the reaction of HO^- ions with Zn(II) species to form ZnO. When the steady-state growth is reached, the pH value, denoted here as the steady-state pH, is much lower than the pH_0, reaching a fairly constant value

at the growth temperature of 85 °C. While the pH_0 is varied from 7.1 to 11.0 for a given $[Ga(NO_3)_3]$ / $[Zn(NO_3)_2]$ ratio, it is worth noticing that the steady-state pH lies in the lower range of 5.8 to 9.2, as shown in **Figure 3a**. In contrast, the steady-state pH is relatively independent upon the $[Ga(NO_3)_3]$ / $[Zn(NO_3)_2]$ ratio for a given pH_0 and its value is around 8.75, as revealed in **Figure 3b**.

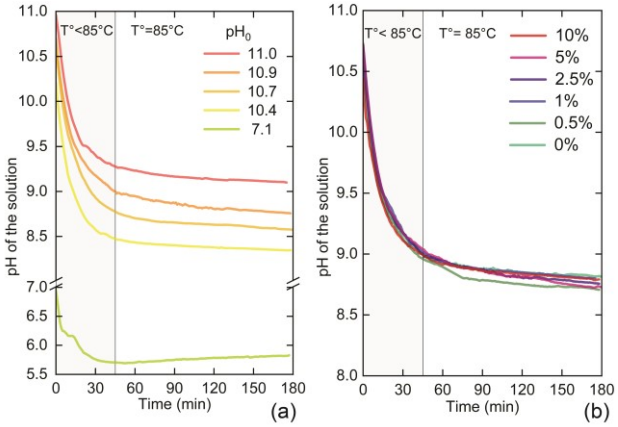

Figure 3. *In situ* measurements of the pH during the CBD of ZnO NWs (a) for pH_0 values in the range of 7.1-11.0 and for a given $[Ga(NO_3)_3]$ / $[Zn(NO_3)_2]$ ratio of 5 % as well as (b) for $[Ga(NO_3)_3]$ / $[Zn(NO_3)_2]$ ratio values in the range of 0-10 % and for a given pH_0 of 10.9.

Thermodynamic computations yielding theoretical solubility plot and speciation diagrams of Zn(II) species were carried out using Visual MINTEQ software. The theoretical solubility plot of Zn(II) species as a function of the calculated pH is presented in **Figure 4a** for a given $[Ga(NO_3)_3]$ / $[Zn(NO_3)_2]$ ratio of 5 %. The calculated pH was deduced from mass and charge equilibrium balances at 85 °C for each data point by fixing the NH_3 concentration in the range of 0-1500 mM. Each data point corresponded to the addition of 1 mM of NH_3 in the chemical bath. The calculated pH basically corresponds to the theoretical equilibrium pH. It should be noted here that it is in very good agreement with the experimental steady-state pH, as represented by colored solid lines, showing the accuracy of the thermodynamic computations. The theoretical solubility plots of Zn(II) species as a function of the calculated pH on a narrower range and for $[Ga(NO_3)_3]$ / $[Zn(NO_3)_2]$ ratios varying from 0 to 10 % are presented in **Figure 4b**. Theoretical speciation diagrams of Zn(II) species as a function of the calculated pH are plotted in **Figure 4c**.

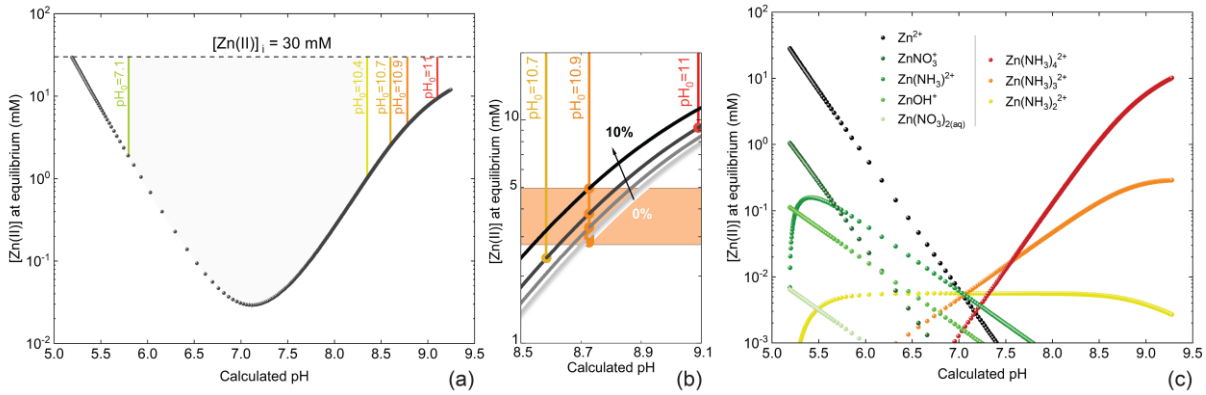

Figure 4. (a) Theoretical solubility plot of Zn(II) species at 85 °C as a function of the calculated pH, each data point corresponding to the addition of 1 mM of NH_3 in the chemical bath. The NH_3 concentration was varied in the range of 0-1500 mM while the $Zn(NO_3)_2$ and $Ga(NO_3)_3$ concentrations were set to 30 and 1.5 mM, respectively. Supersaturation in Zn(II) species is illustrated by colored solid lines placed at the steady-state pH values as shown in Figure 3 and was estimated by the difference between the initial $Zn(NO_3)_2$ concentration of 30 mM and the equilibrium concentration of soluble Zn(II) species. (b) Theoretical solubility plots of Zn(II) species at 85 °C as a function of the calculated pH on a narrower range. The $Zn(NO_3)_2$ concentration was set to 30 mM, while the $Ga(NO_3)_3$ concentration was varied in the range of 0.15 to 3 mM. (c) Speciation diagram of Zn(II) species at 85 °C as a function of the calculated pH, each data point corresponding to the addition of 1 mM of NH_3 in the chemical bath. The NH_3 concentration was varied in the range of 0-1500 mM while the $Zn(NO_3)_2$ concentrations was set to 30 mM.

The growth of ZnO NWs with the preferential elongated shape by CBD is governed by thermodynamic considerations related to surface energy minimization, but driven by kinetics. Supersaturation is a key thermodynamic quantity to be determined because ZnO NWs typically develop over the metastable limit where both homogeneous and heterogeneous growths occur. Supersaturation was estimated here by the difference between the initial $Zn(NO_3)_2$ concentration of 30 mM and the equilibrium concentration of soluble Zn(II) species at 85 °C. In the low calculated pH range from 5.2 to 6.2 where most of the Zn(II) species are Zn^{2+} ions in excess as compared to HO^- ions acting as the limiting reactant following the hydrolysis of HMTA and NH_3, only a few mM of NH_3 drastically increase the pH and thus supersaturation is not straightforward to be monitored. Interestingly, supersaturation is found to progressively decrease in the calculated pH range of 8.0 to 9.5. In other words, as the pH_0 is increased, the decrease in the supersaturation is favorable to strengthen the heterogeneous growth of ZnO NWs on the polycrystalline ZnO seed layer, which is at the expense of the homogeneous growth in aqueous solution. The present statement clearly accounts for the increase in

the length and related deposited volume of ZnO NWs in the pH_0 range of 10.4-11.0, as shown in **Figure 2a**. In this range, $Zn(NH_3)_4^{2+}$ complexes are the predominant stable Zn(II) species and act as the limiting reactant, while HO^- ions are strongly in excess following the hydrolysis of NH_3. The addition of NH_3 is thus a good mean to precisely control the morphology of ZnO NWs. As the pH_0 is further increased to 11.3, Zn(II) species are highly soluble and hence supersaturation is very low, leading to a very low deposited volume of ZnO NWs.

Importantly, the theoretical solubility plot of Zn(II) species depends on the $[Ga(NO_3)_3]$ / $[Zn(NO_3)_2]$ ratio. In particular, supersaturation is found to decrease as the $[Ga(NO_3)_3]$ / $[Zn(NO_3)_2]$ ratio is increased from 0 to 10 %. This further accounts for the increase in the deposited volume of ZnO NWs as the $[Ga(NO_3)_3]$ / $[Zn(NO_3)_2]$ ratio is increased from 0 to 5 % and for a given pH_0 leading to a fairly constant steady-state pH value. As the $[Ga(NO_3)_3]$ / $[Zn(NO_3)_2]$ ratio is further increased to 10 %, supersaturation is much lower and thus the deposited volume of ZnO NWs is also lower. It should also be noted that the increase in the deposited volume follows the increase in the diameter of ZnO NWs, until a 2D layer is formed for the highest $[Ga(NO_3)_3]$ / $[Zn(NO_3)_2]$ ratio, where radial growth is spatially constrained.

Effects of the nature of Ga(III) species in the chemical bath – To understand in more details the physico-chemical processes in the chemical bath, electrostatic interactions between the crystallographic planes of ZnO NWs and Ga(III) soluble species should be considered. The surface electrical charge of ZnO NWs switches from a positive to negative value at a given pH, denoted as the isoelectric point (IEP). The IEP represents the point for which the surface electrical charge is neutral and bares an equal number of positive and negative charges. Correlatively, the point of zero charge (PZC) represents the point for which the surface electrical charge is neutral and does not bare any individual charges. Basically, the values of PZC and IEP strongly depend on the coordination of surface oxygen atoms and of their polarization by the zinc atoms, which are related to the nature of the crystallographic planes of ZnO. Since the concentration of H^+ ions needed for compensating the surface electrical charge is larger for the *c*-plane than for the *m*-plane, the values of PZC and IEP are expected to be higher for the *m*-plane. The PZC was reported to be 10.2 ± 0.2 and 8.7 ± 0.2 for the nonpolar *m*-plane and polar *c*-plane, respectively.[4,24,25] It is thus significantly higher for the *m*-plane sidewalls of ZnO NWs than for their *c*-

plane top facets. Except for the pH_0 of 7.1, in the steady-state pH range that lies in between both PZC values as shown in **Figure 3**, the *c*-plane top facet and *m*-plane sidewalls of ZnO NWs thus have an opposite surface electrical charge. The *c*-plane top facet of ZnO NWs is negatively charged while their *m*-plane sidewalls are still positively charged. Theoretical speciation diagrams of Ga(III) species as a function of the calculated pH and for a given $[Ga(NO_3)_3]$ / $[Zn(NO_3)_2]$ ratio of 5 % were carried out using Visual MINTEQ software and are presented in **Figure 5a**.

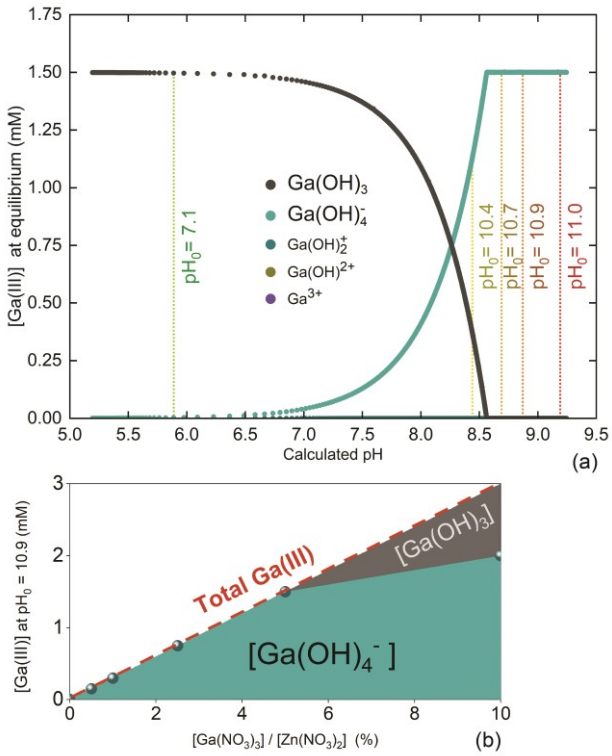

Figure 5. (a) Speciation diagram of Ga(III) species at 85 °C as a function of the calculated pH, each data point corresponding to the addition of 1 mM of NH_3 in the chemical bath. The NH_3 concentration was varied in the range of 0-1500 mM while the $Ga(NO_3)_3$ concentration was set to 1.5 mM. (b) Distribution of $Ga(OH)_3$ and $Ga(OH)_4^-$ complexes as a function of the $[Ga(NO_3)_3]$ / $[Zn(NO_3)_2]$ ratio for a given pH_0 of 10.9.

The majority soluble Ga(III) species changes from $Ga(OH)_3$ complexes in the low calculated pH range to $Ga(OH)_4^-$ complexes in the high calculated pH range. Other Ga(III) species are strongly in a minority. Additional theoretical speciation diagrams of Ga(III) species as a function of the calculated pH were computed for a given pH_0 of 10.9 and for $[Ga(NO_3)_3]$ / $[Zn(NO_3)_2]$ ratios in the range of 0-10 %, from which the distribution of $Ga(OH)_3$ and $Ga(OH)_4^-$ complexes was inferred. Similarly, $Ga(OH)_4^-$ complexes are clearly the predominant Ga(III) soluble species, regardless of the $[Ga(NO_3)_3]$ /

[$Zn(NO_3)_2$] ratio. These $Ga(OH)_4^-$ complexes adsorb on the positively-charged *m*-plane sidewalls of ZnO NWs following attractive electrostatic interactions and hence act as capping agents. Importantly, the $Ga(OH)_4^-$ complex concentration continuously increases with the [$Ga(NO_3)_3$] / [$Zn(NO_3)_2$] ratio, as indicated in **Figure 5b**, correlatively resulting in the increase in the diameter of ZnO NWs and in the decrease in their aspect ratio, as shown in **Figure 2b**. In contrast to $Al(OH)_4^-$ complexes that inhibit the radial growth of ZnO NWs in the same steady-state pH range,[5] $Ga(OH)_4^-$ complexes strongly enhance the development of the *m*-plane sidewalls of ZnO NWs. Gallium is expected to act as a stable surfactant on the subsurface of the *m*-plane sidewalls, as previously reported by density functional theory (DFT) calculations,[26] in turn promoting the radial growth of ZnO NWs. Also, the surface energy of the nonpolar *m*-planes has been found, from DFT calculations, to be drastically increased when Ga atoms replace surface Zn atoms.[27] This may favor the formation of ZnO NWs with a less elongated shape following thermodynamic considerations. $Ga(OH)_4^-$ complexes further result in the growth of ZnO NWs with a pencil-like shape on their tip originating from the formation of inclined top facets. The inclination angle of the top facet is about 55 °, as presented in **Figure S2**, presumably indicating the formation of semipolar (11-2-2) planes. Also, it should be noted that these ZnO NWs do not exhibit the presence of extended defects such as twins or stacking faults in their center.

Effects of the pH_0 of the solution and of the $Ga(NO_3)_3$ Relative Concentration on the Incorporation and Doping Mechanisms of Gallium into ZnO Nanowires

Gallium content measurements by chemical analyses - The Ga content into ZnO NW arrays was assessed by XRD and FESEM-EDS measurements. Only the wurtzite crystallographic structure of the ZnO seed layer and NWs arise from the XRD patterns in **Figure S3**, showing no formation of any crystallographic phases related to Ga_2O_3 and $ZnGa_2O_4$. The present statement is in agreement with the formation enthalpy of Ga_2O_3 (*i.e.*, -260 kcal/mol) as compared to the formation enthalpy of ZnO (*i.e.*, -83 kcal/mol). All FESEM-EDS acquisition parameters were identical, and all related spectra as presented in **Figure 6** were normalized with respect to the Zn K_β line pointed at 9.57 keV. In the range of 9-10 keV, the Ga K_α line at 9.25 keV occurs with a similar intensity when ZnO NWs are grown at a pH_0 ranging from 10.4 to 11.0 and for a [$Ga(NO_3)_3$] / [$Zn(NO_3)_2$] ratio of 5 % and hence regardless of

their structural morphology. In contrast, no Ga K_α line is revealed when ZnO NWs are grown at the lower pH_0 of 7.1 and for a $[Ga(NO_3)_3]$ / $[Zn(NO_3)_2]$ ratio of 5 %. Eventually, the deposited volume of ZnO NWs when grown at the pH_0 of 11.3 was too small to be characterized. Following a semi-quantitative analysis of the present FESEM-EDS spectra in **Figure 6a**, the Ga / Zn element ratio in ZnO NWs lies in the narrow range of 1.8 to 2.8 %, regardless of the pH_0 ranging from 10.4 to 11.0.

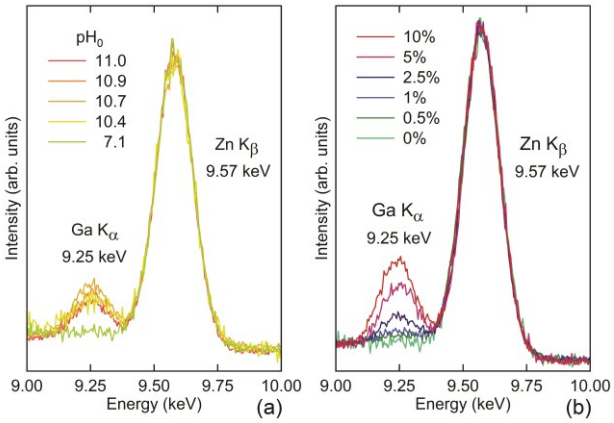

Figure 6. (a) FESEM-EDS spectra of ZnO NWs grown with pH_0 values in the range of 7.1-11.0 and for a given $[Ga(NO_3)_3]$ / $[Zn(NO_3)_2]$ ratio of 5 %. (b) FESEM-EDS spectra of ZnO NWs grown with $[Ga(NO_3)_3]$ / $[Zn(NO_3)_2]$ ratio values in the range of 0-10 % and for a given pH_0 of 10.9. All the spectra were normalized with respect to the Zn K_β line pointed at 9.57 keV.

Very interestingly, the intensity of the Ga K_α line at 9.25 keV in ZnO NWs progressively increases as the $[Ga(NO_3)_3]$ / $[Zn(NO_3)_2]$ ratio is increased from 0 to 10 % and for a given pH_0 of 10.9. Following a semi-quantitative analysis of the present FESEM-EDS spectra in **Figure 6b**, the Ga / Zn element ratio in ZnO NWs continuously increases from 0.2 to 4.5 % as the $[Ga(NO_3)_3]$ / $[Zn(NO_3)_2]$ ratio is increased from 0 to 10 %, as presented in **Figure 7**. More accurate EDS measurements of the Ga / Zn element ratio were obtained in a STEM on single ZnO NWs. From each ZnO NW array grown with a $[Ga(NO_3)_3]$ / $[Zn(NO_3)_2]$ ratio of 0.5, 2.5, and 10 %, at least 5 single NWs were analyzed after their dispersion on a copper grid. Both EDS single point and map measurements were collected at different positions of the NWs. Since Ga and Zn elements have a different x-ray absorption coefficient, a correction in diameter was applied for each single NW based on the TEM diameter measurement. Similarly to FESEM-EDS measurements, the Ga / Zn element ratio in the single ZnO NWs continuously increases from 0.3 to more than 4 % as the $[Ga(NO_3)_3]$ / $[Zn(NO_3)_2]$ ratio is increased from 0.5 to 10 %, as presented in **Figure**

7. However, it is worth noticing that the increase in the Ga / Zn element ratio with the $[Ga(NO_3)_3]$ / $[Zn(NO_3)_2]$ ratio is not perfectly linear. This can directly be correlated with the increase in the $Ga(OH)_4^-$ concentration with the $[Ga(NO_3)_3]$ / $[Zn(NO_3)_2]$ ratio as shown in **Figure 5b**, the deviation from linearity being accounted for by the progressive formation of $Ga(OH)_3$ complexes at the largest $[Ga(NO_3)_3]$ / $[Zn(NO_3)_2]$ ratio of 10 %. Only two third of the Ga(III) species in the chemical bath are $Ga(OH)_4^-$ complexes for the $[Ga(NO_3)_3]$ / $[Zn(NO_3)_2]$ ratio of 10 %. The solubility limit of Ga into ZnO NWs may also be reached close to the present value, which is in the same order as the solubility limit of Ga of 2.7 % into ZnO powders.[28] Interestingly, the spatial distribution of Ga atoms into the ZnO NWs turns out to be homogeneous, as revealed by the STEM-EDS elemental maps of ZnO NWs grown with a $[Ga(NO_3)_3]$ / $[Zn(NO_3)_2]$ ratio of 0.5 % and for a pH_0 of 10.9 in the inset of **Figure 7**.

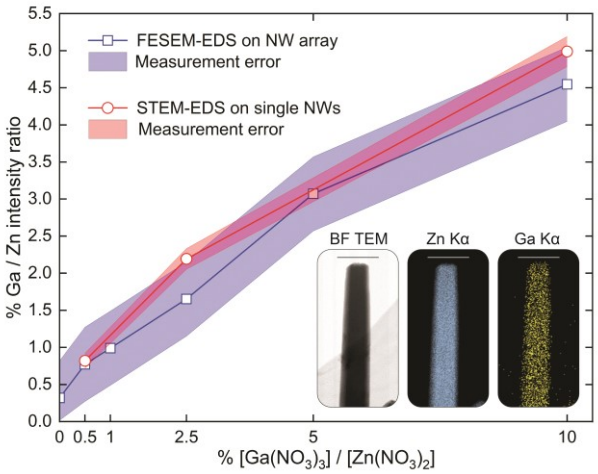

Figure 7. Evolution of the Ga / Zn element ratio in ZnO NWs as a function of the $[Ga(NO_3)_3]$ / $[Zn(NO_3)_2]$ ratio and for a given pH_0 of 10.9, as inferred from FESEM-EDS and STEM-EDS measurements. The insets are bright-field TEM image and STEM-EDS elemental maps of the Zn (blue) and Ga (yellow) elements, respectively, collected on a single ZnO NW grown with a $[Ga(NO_3)_3]$ / $[Zn(NO_3)_2]$ ratio of 0.5 % and for a given pH_0 of 10.9. The scale bar is 250 nm.

Ga incorporation measurements by optical analyses

Following the chemical analysis, the Ga content into ZnO NWs was found to be high. Besides its presence on the surfaces of ZnO NWs, this suggests its massive incorporation in an homogeneous and controllable manner, provided that the pH_0 lies in the range of 10.4-11.3 and by varying the $[Ga(NO_3)_3]$ / $[Zn(NO_3)_2]$ ratio. However, to induce an efficient incorporation and related doping of ZnO NWs, these Ga atoms must be incorporated on dedicated sites in the ZnO lattice, namely they should substitute for

Zn atoms to form Ga_{Zn}. In order to investigate in more details the Ga incorporation mechanisms, Raman scattering spectra of ZnO NWs are presented in **Figure 8**.

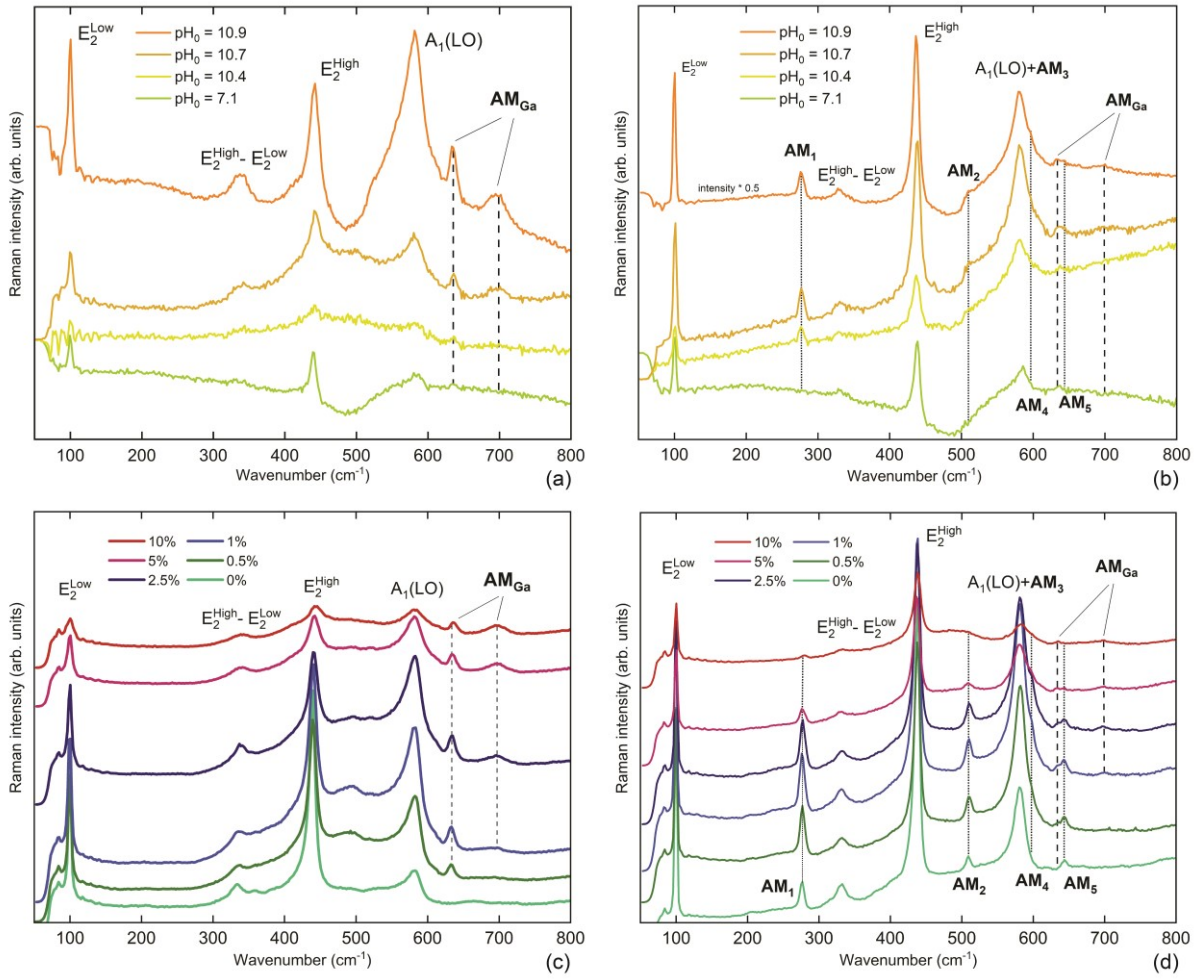

Figure 8. Raman spectra of ZnO NWs grown with pH_0 values in the range of 7.1-11.0 and for a given $[Ga(NO_3)_3]$ / $[Zn(NO_3)_2]$ ratio of 5 %, (a) before and (b) after annealing at 500 °C for 1 h under oxygen atmosphere. Raman spectra of ZnO NWs grown with $[Ga(NO_3)_3]$ / $[Zn(NO_3)_2]$ ratio values in the range of 0-10 % and for a given pH_0 of 10.9, (c) before and (d) after annealing at 500 °C for 1 h under oxygen atmosphere.

In the backscattering configuration with laser light propagation along the *c*-axis, only three Raman modes are characteristics of the wurtzite structure of ZnO NWs. The Raman lines at 100, 437-443 and 574 cm^{-1} are attributed to E_2(low), E_2(high), and A_1(LO) modes, respectively.[29] The second-order Raman line at 333 cm^{-1} corresponds to the E_2(high)-E_2(low) mode. Notably, except for ZnO NWs grown at the pH_0 of 7.1 and at the $[Ga(NO_3)_3]$ / $[Zn(NO_3)_2]$ ratio of 0 % in which no Ga atoms were revealed by chemical analyses, two Ga-related additional modes (AM_{Ga}) at 633.5 and 696.1 cm^{-1} occur in as-grown ZnO NWs, as revealed in **Figure 8a,c**. Those Raman lines have previously been reported in Ga-doped

ZnO [11,19,27,30,31] and are attributed to Ga-related point defects. In contrast, the peak at 633.5 cm^{-1} cannot be assigned to the $A_g^{(8)}$ vibrational mode of the β-Ga_2O_3 phase at 630 cm^{-1}, because all other A_g modes of β-Ga_2O_3 are not observed.[32,33,34] The relative intensities of the AM_{Ga} at 633.5 and 696.1 cm^{-1} with respect to the E_2(high) mode do not likely depend on the pH_0 in the range of 10.4-11.0, as revealed in **Figure 8a**. In contrast, they continuously increase as the $[Ga(NO_3)_3]$ / $[Zn(NO_3)_2]$ ratio is increased from 0 to 10 % and thus as the Ga / Zn element ratio is increased from 0 to 4 %, as shown in **Figure 8c** and **S4**. It is additional strong evidence that these AM_{Ga} are directly attributed to Ga-related point defects. Since Ga interstitials (Ga_I) typically have a high formation energy and thus are unlikely to form in ZnO,[35] both AM_{Ga} are expected to be due to the incorporation of Ga_{Zn} into ZnO NWs. Importantly, except for ZnO NWs grown at the pH_0 of 7.1, the intensities of the AM_{Ga} strongly decrease after annealing under oxygen atmosphere as presented in **Figure 8b,d**. This is not related to an exo-diffusion of Ga atoms, because the Ga / Zn element ratio retains a constant value as shown in **Figure S5**. Conversely, standard additional modes occur at 277 (AM_1), 510 (AM_2), 581 (AM_3), 597 (AM_4), and 643 (AM_5) cm^{-1} after annealing under oxygen atmosphere as presented in **Figure 8b,d**. These AMs have widely been reported when ZnO was doped with various elements such as N, Fe, Sb, Al, and Ga, despite their different mass and size. Accordingly, the standard AMs have been attributed either to dopant-induced defects in the host lattice (such as Zn_i[36], Zn_i clusters[37], or Zn_i-Al_{Zn} complexes[38]) and/or to silent ZnO B_1 modes which become Raman active due to a local breakdown of the translational symmetry[39,40] when the lattice is distorted. The AM_{Ga} still occur after annealing under oxygen atmosphere, but with a much lower intensity, indicating the presence of Ga_{Zn}. Temperature-dependent Raman spectra of ZnO NWs grown by CBD for a pH_0 of 10.9 and for a $[Ga(NO_3)_3]$ / $[Zn(NO_3)_2]$ ratio of 2.5 % are presented in **Figure 9**.

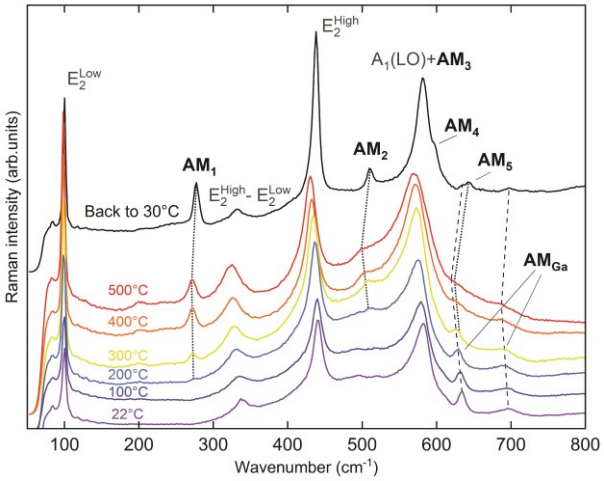

Figure 9. Raman spectra of ZnO NWs grown with a pH_0 of 10.9 and a $[Ga(NO_3)_3]$ / $[Zn(NO_3)_2]$ ratio of 2.5 %, as collected from room temperature to 500 °C under oxygen atmosphere.

The intensities of the AM_{Ga} are fairly constant from room temperature to 200 °C. As the temperature is further raised from 200 to 400 °C, the intensities of the AM_{Ga} strongly decrease until almost vanishing while the standard AMs arise at 200 °C and their intensities strongly increase until 400 °C. The Raman spectrum collected at room temperature after annealing under oxygen atmosphere both involves the presence of standard AMs with a high intensity and residual AM_{Ga} with a very low intensity. This clearly indicates that a significant part of Ga atoms incorporated into ZnO NWs in the form of Ga_{Zn} is most likely converted into a new type of defects during annealing under oxygen atmosphere, while remaining in the ZnO lattice.

Moreover, the position of the E_2(high) line of as-grown ZnO NWs shifts towards higher wavenumber from 439 to 443.5 cm^{-1} as the $[Ga(NO_3)_3]$ / $[Zn(NO_3)_2]$ ratio is increased from 0 to 10 % for a given pH_0 of 10.9, as shown in **Figure 10a**. After annealing under oxygen atmosphere, the E_2(high) line shifts back near the position of undoped ZnO NWs (437.5 cm^{-1}), as depicted in **Figure 10b**. The E_2(high) mode is related to the vibration of the oxygen sub-lattice and is very sensitive to the strain, shifting towards higher wavenumber when the ZnO lattice is under a compressive stress state.[41,42] This shows that the Ga incorporation in the form of Ga_{Zn} into as-grown ZnO NWs is responsible for the generation of a large strain in the ZnO lattice that further relaxes after annealing under oxygen atmosphere.

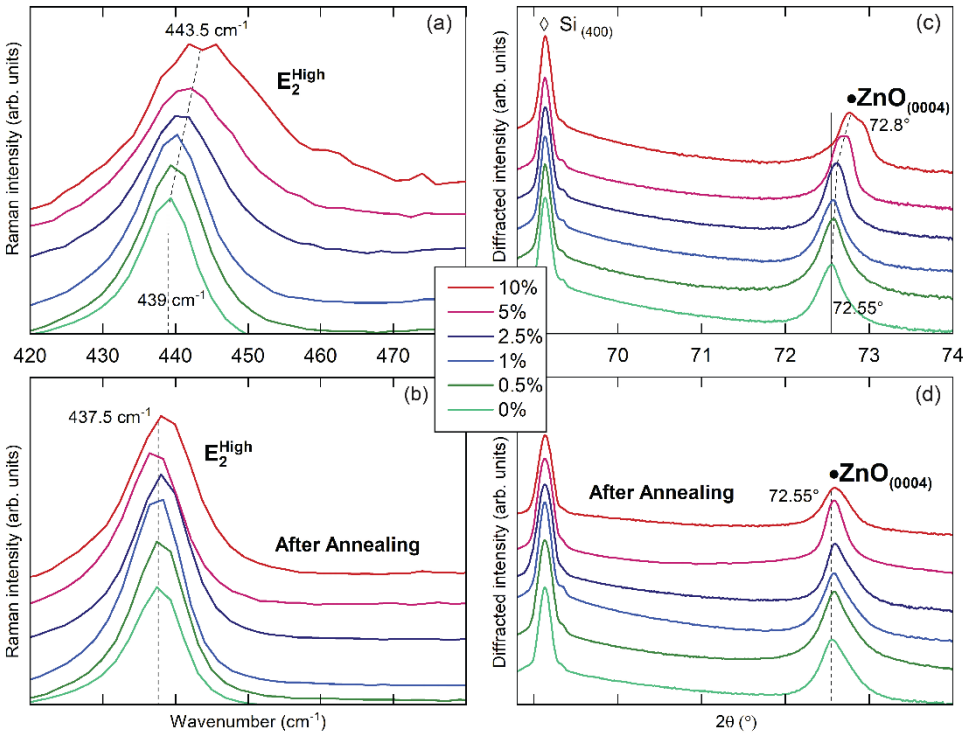

Figure 10. (a,b) Raman spectra and (c,d) XRD patterns of ZnO NWs grown with $[Ga(NO_3)_3]$ / $[Zn(NO_3)_2]$ ratio values in the range of 0-10 % and for a given pH_0 of 10.9; (a, c) before and (b, d) after annealing at 500 °C for 1 h under oxygen atmosphere. The position in the XRD patterns was precisely calibrated on the Si (400) peak pointing at 2θ = 69.13 °.

Correlatively, the (0004) diffraction peak of as-grown ZnO NWs shifts from 72.55 to 72.8 ° as the $[Ga(NO_3)_3]$ / $[Zn(NO_3)_2]$ ratio is increased from 0 to 10 % for a given pH_0 of 10.9, as shown in **Figure 10c**. From cell refinement, the *c*-lattice parameter of as-grown ZnO NWs is found to decrease from 5.208 to 5.194 Å for a $[Ga(NO_3)_3]$ / $[Zn(NO_3)_2]$ ratio of 0 and 10 %, respectively, which is in agreement with Refs. [12]-[15]. A similar lattice distortion of as-grown ZnO NWs also occurs regardless of the pH_0 from 10.4 to 11.0, except for the pH_0 of 7.1 as seen in **Figure S3d**, which confirms that the decrease in the *c*-lattice parameter is directly due to the progressive Ga incorporation in the form of Ga_{Zn} with a larger amount, regardless of the morphology of ZnO NWs. Ga_{Zn} is well-known to induce a decrease in the *c*-lattice parameter of ZnO powder as well, which was explained by valence bond representations.[43] Interestingly, after annealing under oxygen atmosphere, the (0004) diffraction peak shifts back close to the position of bulk ZnO, as revealed in **Figure 10d**. However, the *c*-lattice parameter is still slightly smaller in ZnO NWs grown with a $[Ga(NO_3)_3]$ / $[Zn(NO_3)_2]$ ratio ranging from 0.5 to 10 %, as compared

to the undoped ZnO NWs, revealing the presence of a small residual strain in ZnO NWs after annealing under oxygen atmosphere. Notably, the standard AMs form during the strain relaxation, such that they are most likely caused by dopant-induced defects in the host lattice.[34-38]

Ga incorporation mechanisms

These experimental observations suggest the following Ga incorporation mechanisms into ZnO NWs following the CBD and post-deposition annealing under oxygen atmosphere. Owing to the adsorption of $Ga(OH)_4^-$ complexes as capping agents on the sidewalls of ZnO NWs at a pH_0 from 10.4, a large amount of Ga atoms as measured by chemical analyses occurs in ZnO NWs. It is expected that a significant part of Ga atoms is located on the surface of ZnO NWs, or more likely on the sub-surface of the *m*-plane sidewalls as shown in Ref. 26, promoting in turn their radial growth as shown in **Figure 2b**. Additionally, another significant part of Ga atoms is most likely located in tetrahedral sites of the host lattice in the form of Ga_{Zn} acting as shallow donors, inducing the presence of the AM_{Ga} in Raman spectra in **Figures 8** and **9** as well as generating a drastic strain level as revealed in **Figure 10**. The formation energy of Ga_{Zn} is indeed low on a broad range of oxygen chemical potential, especially as compared to other native point defects such as zinc vacancies (V_{Zn}) or oxygen interstitials (O_i).[35] Following the post-deposition annealing under oxygen atmosphere, Ga_{Zn} result, to a significant part, in the formation of Ga_{Zn}-V_{Zn} complexes acting as compensating acceptors, which is indicated by the decrease/vanishing of the AM_{Ga} modes at the benefit of the occurrence/increase of the standard AM modes in **Figures 8** and **9**. Under oxygen-rich conditions (*i.e.* high oxygen chemical potential) and when the Fermi level approaches the conduction band minimum, the formation energy of Ga_{Zn}-V_{Zn} complexes is indeed lower than the formation energy of Ga_{Zn} in addition to any other native point defects.[35] Ga_{Zn}-V_{Zn} complexes are also expected to induce a significant lattice relaxation, in turn relaxing the strain level in ZnO NWs as shown in **Figure 10**.

CONCLUSIONS

A combined investigation involving a theoretical thermodynamic and experimental approach has been carried out to elucidate the formation and Ga incorporation mechanisms of ZnO NWs grown by CBD. The addition of ammonia to tune the pH_0 of the solution from 7.1 to 11.3 and of $Ga(NO_3)_3$ to tailor the

$[Ga(NO_3)_3]$ / $[Zn(NO_3)_2]$ ratio in the range of 0-10 % has been achieved to reveal their effects on the structural morphology of ZnO NWs as well as on the Ga incorporation following chemical and optical analyses. From speciation diagrams of Ga(III) species, we show that $Ga(OH)_4^-$ complexes are preferentially formed over the high pH range and adsorb on the *m*-plane sidewalls of ZnO NWs to act as capping agents following attractive electrostatic interactions, which promotes their development and the related radial growth. From theoretical solubility plots, we reveal that the deposited volume and correlated length of ZnO NWs is directly explained by the supersaturation in the chemical bath, which is dependent upon both the $[Ga(NO_3)_3]$ / $[Zn(NO_3)_2]$ ratio and pH_0 of the growth solution. This allows us to simultaneously engineer the shape and dimensions of ZnO NWs while incorporating a given Ga content in their center. The Ga incorporation mechanisms into ZnO NWs following the CBD process and post-deposition annealing have been shown from EDS and Raman scattering measurements, where the AM_{Ga} and standard AM lines appear as fingerprints of the behaviour of Ga atoms into the host lattice. The predominant AM_{Ga} at 633.5 and 696.1 cm^{-1} in as-grown ZnO NWs are attributed to the incorporation of Ga_{Zn}, acting as shallow donors and further generating a drastic strain. Following the post-deposition annealing under oxygen atmosphere, the standard AMs at 277, 510, 581, 597, and 643 cm^{-1} in annealed ZnO NWs are assigned to the formation of Ga_{Zn}-V_{Zn} complexes, acting as compensating acceptors and additionally relaxing the strain level. A significant part of Ga_{Zn} in as-grown ZnO NWs is thus converted into Ga_{Zn}-V_{Zn} complexes in annealed ZnO NWs. These findings report an in-depth understanding of the formation and Ga incorporation mechanisms of ZnO NWs by CBD, which can be applied to a vast number of extrinsic doping elements for carefully governing the physical properties as a further essential issue in nanoscale engineering devices.

ACKNOWLEDGMENTS

The authors would like to thank Hervé Roussel from LMGP, Grenoble, France, for his assistance in the XRD experiments. The authors acknowledge the financial support by the French Research National Agency through the projects DOSETTE (ANR-17-CE24-0004) and ROLLER (ANR-17-CE09-0033). P.G. was supported by a doctoral fellowship from the CDP Eco-SESA (ANR-15-IDEX-02). The authors further acknowledge the facilities, and the scientific and technical assistance of the CMTC

characterization platform of Grenoble INP, which is supported by the Centre of Excellence of Multifunctional Architectured Materials (LabEx CEMAM) under the contract ANR-10-LABX-44-01 funded by the "Investments for the Future" Program. Funding by the Carnot Institute Energies du Futur through the project ECOLED is also acknowledged.

SUPPORTING INFORMATION

FESEM images of the tips of ZnO NWs **(Figure S1)**; HRTEM and TEM images of ZnO NWs (**Figure S2**); XRD patterns of ZnO NWs (**Figure S3**); Evolution of the AM_{Ga} / E_2(high) intensity ratio as a function of $[Ga(NO_3)_3]$ / $[Zn(NO_3)_2]$ ratio in as-grown ZnO NWs (**Figure S4**); FESEM-EDS spectra of ZnO NWs before and after annealing under oxygen atmosphere (**Figure S5**).

REFERENCES

(1) Xu, S.; Wang, Z. L. One-Dimensional ZnO Nanostructures : Solution Growth and Functional Properties. *Nano Res.* **2011**, *4* (11), 1013–1098.

(2) Wei, Y.; Wu, W.; Guo, R.; Yuan, D.; Das, S.; Wang, Z. L. Wafer-Scale High-Throughput Ordered Growth of Vertically Aligned ZnO Nanowire Arrays. *Nano Lett.* **2010**, *10* (9), 3414–3419.

(3) Consonni, V.; Sarigiannidou, E.; Appert, E.; Bocheux, A.; Guillemin, S.; Donatini, F.; Robin, I.-C.; Kioseoglou, J.; Robaut, F. Selective Area Growth of Well-Ordered ZnO Nanowire Arrays with Controllable Polarity. *ACS Nano* **2014**, *8* (5), 4761–4770.

(4) Joo, J.; Chow, B. Y.; Prakash, M.; Boyden, E. S.; Jacobson, J. M. Face-Selective Electrostatic Control of Hydrothermal Zinc Oxide Nanowire Synthesis. *Nat. Mater.* **2011**, *10* (8), 596–601.

(5) Verrier, C.; Appert, E.; Chaix-Pluchery, O.; Rapenne, L.; Rafhay, Q.; Kaminski-Cachopo, A.; Consonni, V. Tunable Morphology and Doping of ZnO Nanowires by Chemical Bath Deposition Using Aluminum Nitrate. *J. Phys. Chem. C* **2017**, *121* (6), 3573–3583.

(6) Verrier, C.; Appert, E.; Chaix-Pluchery, O.; Rapenne, L.; Rafhay, Q.; Kaminski-Cachopo, A.; Consonni, V. Effects of the PH on the Formation and Doping Mechanisms of ZnO Nanowires Using Aluminum Nitrate and Ammonia. *Inorg. Chem.* **2017**, *56* (21), 13111–13122.

(7) Gabás, M.; Landa-Cánovas, A.; Luis Costa-Krämer, J.; Agulló-Rueda, F.; González-Elipe, A.

R.; Díaz-Carrasco, P.; Hernández-Moro, J.; Lorite, I.; Herrero, P.; Castillero, P.; Barranco, A.; Ramón Ramos-Barrado, J. Differences in N-Type Doping Efficiency between Al- and Ga-ZnO Films. *J. Appl. Phys.* **2013**, *113* (16), 163709.

(8) Wang, H.; Baek, S.; Song, J.; Lee, J.; Lim, S. Microstructural and Optical Characteristics of Solution-Grown Ga-Doped ZnO Nanorod Arrays. *Nanotechnology* **2008**, *19* (7), 075607.

(9) Escobedo-Morales, A.; Pal, U. Defect Annihilation and Morphological Improvement of Hydrothermally Grown ZnO Nanorods by Ga Doping. *Appl. Phys. Lett.* **2008**, *93* (19), 1–4.

(10) Lee, J.-H.; Lee, K. Y.; Kumar, B.; Kim, S.-W. Synthesis of Ga-Doped ZnO Nanorods Using an Aqueous Solution Method for a Piezoelectric Nanogenerator. *J. Nanosci. Nanotechnol.* **2012**, *12* (4), 3430–3433.

(11) Pineda-Hernández, G.; Escobedo-Morales, A.; Pal, U.; Chigo-Anota, E. Morphology Evolution of Hydrothermally Grown ZnO Nanostructures on Gallium Doping and Their Defect Structures. *Mater. Chem. Phys.* **2012**, *135* (2–3), 810–817.

(12) Kim, S.; Nam, G.; Park, H.; Yoon, H.; Lee, S.; Kim, J. S. Effects of Doping with Al , Ga , and In on Structural and Optical Properties of ZnO Nanorods Grown by Hydrothermal Method. *Bull. Korean Chem. Soc.* **2013**, *34* (4), 1205–1211.

(13) Park, G. C.; Hwang, S. M.; Choi, J. H.; Kwon, Y. H.; Cho, H. K.; Kim, S. W.; Lim, J. H.; Joo, J. Effects of In or Ga Doping on the Growth Behavior and Optical Properties of ZnO Nanorods Fabricated by Hydrothermal Process. *Phys. Status Solidi Appl. Mater. Sci.* **2013**, *210* (8), 1552–1556.

(14) Park, G. C.; Hwang, S. M.; Lim, J. H.; Joo, J. Growth Behavior and Electrical Performance of Ga-Doped ZnO Nanorod/p-Si Heterojunction Diodes Prepared Using a Hydrothermal Method. *Nanoscale* **2014**, *6* (3), 1840–1847.

(15) Lim, J. H.; Lee, S. M.; Kim, H.-S.; Kim, H. Y.; Park, J.; Jung, S.-B.; Park, G. C.; Kim, J.; Joo, J. Synergistic Effect of Indium and Gallium Co-Doping on Growth Behavior and Physical Properties of Hydrothermally Grown ZnO Nanorods. *Sci. Rep.* **2017**, *7* (December 2016), 41992.

(16) Li, R.; Yu, C.; Dong, H.; Jia, W.; Li, T.; Zhang, Z.; Xu, B. Effects of $Ga_x Zn_{1-x}O$ Nanorods on

the Photoelectric Properties of N-ZnO Nanorods/p-GaN Heterojunction Light-Emitting Diodes. *RSC Adv.* **2017**, *7* (78), 49613–49617.

(17) Saravanakumar, S.; Escobedo-Morales, A.; Pal, U.; Aranda, R. J.; Saravanan, R. Doping-Induced Electron Density Modification at Lattice Sites of ZnO:Ga Nanostructures: Effects on Vibrational and Optical Properties. *J. Mater. Sci.* **2014**, *49* (16), 5529–5536.

(18) Singh, P.; Simanjuntak, F. M.; Kumar, A.; Tseng, T. Y. Resistive Switching Behavior of Ga Doped ZnO-Nanorods Film Conductive Bridge Random Access Memory. *Thin Solid Films* **2018**, *660* (November 2017), 828–833.

(19) Bundesmann, C.; Ashkenov, N.; Schubert, M.; Spemann, D.; Butz, T.; Kaidashev, E. M.; Lorenz, M.; Grundmann, M. Raman Scattering in ZnO Thin Films Doped with Fe, Sb, Al, Ga, and Li. *Appl. Phys. Lett.* **2003**, *83* (10), 1974–1976.

(20) Greene, L. E.; Law, M.; Tan, D. H.; Montano, M.; Goldberger, J.; Somorjai, G.; Yang, P. General Route to Vertical ZnO Nanowire Arrays Using Textured ZnO Seeds. *Nano Lett.* **2005**, *5* (7), 1231–1236.

(21) Cossuet, T.; Roussel, H.; Chauveau, J. M.; Chaix-Pluchery, O.; Thomassin, J. L.; Appert, E.; Consonni, V. Well-Ordered ZnO Nanowires with Controllable Inclination on Semipolar ZnO Surfaces by Chemical Bath Deposition. *Nanotechnology* **2018**, *29* (47), 475601.

(22) Guillemin, S.; Parize, R.; Carabetta, J.; Cantelli, V.; Albertini, D.; Gautier, B.; Brémond, G.; Fong, D. D.; Renevier, H.; Consonni, V. Quantitative and Simultaneous Analysis of the Polarity of Polycrystalline ZnO Seed Layers and Related Nanowires Grown by Wet Chemical Deposition. *Nanotechnology* **2017**, *28* (9), 095704.

(23) Parize, R.; Garnier, J.; Chaix-Pluchery, O.; Verrier, C.; Appert, E.; Consonni, V. Effects of Hexamethylenetetramine on the Nucleation and Radial Growth of ZnO Nanowires by Chemical Bath Deposition. *J. Phys. Chem. C* **2016**, *120* (9), 5242–5250.

(24) Kunze, C.; Valtiner, M.; Michels, R.; Huber, K.; Grundmeier, G. Self-Localization of Polyacrylic Acid Molecules on Polar ZnO(0001)–Zn Surfaces. *Phys. Chem. Chem. Phys.* **2011**, *13* (28), 12959.

(25) Valtiner, M.; Borodin, S.; Grundmeier, G. Stabilization and Acidic Dissolution Mechanism of Single-Crystalline ZnO(0001) Surfaces in Electrolytes Studied by in-Situ AFM Imaging and Ex-Situ LEED. *Langmuir* **2008**, *24* (10), 5350–5358.

(26) Sallet, V.; Sartel, C.; Hassani, S.; Vilar, C.; Amiri, G.; Lusson, A.; Jomard, F.; Galtier, P.; Lefebvre, I.; Delerue, C.; Hamza, M. K.; Canut, B.; Masenelli, B. Crystal Facet Engineering in Ga-Doped ZnO Nanowires for Mid-Infrared Plasmonics. *Cryst. Growth Des.* **2018**, *18* (8), 4287–4295.

(27) Sohn, J. I.; Hong, W. K.; Lee, S.; Lee, S.; Ku, J.; Park, Y. J.; Hong, J.; Hwang, S.; Park, K. H.; Warner, J. H.; Cha, S.; Kim, J. M. Surface Energy-Mediated Construction of Anisotropic Semiconductor Wires with Selective Crystallographic Polarity. *Sci. Rep.* **2014**, *4*, 5680.

(28) Wang, R.; Sleight, A. W.; Cleary, D. High Conductivity in Gallium-Doped Zinc Oxide Powders. *Chem. Mater.* **1996**, *8* (2), 433–439.

(29) Cuscó, R.; Alarcón-Lladó, E.; Ibáñez, J.; Artús, L.; Jiménez, J.; Wang, B.; Callahan, M. J. Temperature Dependence of Raman Scattering in ZnO. *Phys. Rev. B Condens. Matter Mater. Phys.* **2007**, *75* (16), 165202.

(30) Gabás, M.; Díaz-Carrasco, P.; Agulló-Rueda, F.; Herrero, P.; Landa-Cánovas, A. R.; Ramos-Barrado, J. R. High Quality ZnO and Ga:ZnO Thin Films Grown onto Crystalline Si (1 0 0) by RF Magnetron Sputtering. *Sol. Energy Mater. Sol. Cells* **2011**, *95* (8), 2327–2334.

(31) Lung, C.; Toma, M.; Pop, M.; Marconi, D.; Pop, A. Characterization of the Structural and Optical Properties of ZnO Thin Films Doped with Ga, Al and (Al+Ga). *J. Alloys Compd.* **2017**, *725*, 1238–1243.

(32) Onuma, T.; Fujioka, S.; Yamaguchi, T.; Itoh, Y.; Higashiwaki, M.; Sasaki, K.; Masui, T.; Honda, T. Polarized Raman Spectra in β-Ga_2O_3 Single Crystals. *J. Cryst. Growth* **2014**, *401*, 330–333.

(33) Kranert, C.; Sturm, C.; Schmidt-Grund, R.; Grundmann, M. Raman Tensor Elements of Beta-Ga_2O_3. *Sci. Rep.* **2016**, *6*, 35964.

(34) Rao, R.; Rao, A. M.; Xu, B.; Dong, J.; Sharma, S.; Sunkara, M. K. Blueshifted Raman Scattering and Its Correlation with the [110] Growth Direction in Gallium Oxide Nanowires. *J. Appl. Phys.*

2005, *98* (9), 094312.

(35) Demchenko, D. O.; Earles, B.; Liu, H. Y.; Avrutin, V.; Izyumskaya, N.; Ozgur, U.; Morkoc, H. Impurity Complexes and Conductivity of Ga-Doped ZnO. *Phys. Rev. B Condens. Matter Mater. Phys.* **2011**, *075201*, 1–5.

(36) Hu, Y. M.; Li, J. Y.; Chen, N. Y.; Chen, C. Y.; Han, T. C.; Yu, C. C. Correlation between Defect-Related Photoluminescence Emission and Anomalous Raman Peaks in N-Al Co-Doped ZnO Thin Films. *Appl. Phys. Lett.* **2017**, *110* (14), 141903.

(37) Gluba, M. A.; Nickel, N. H.; Karpensky, N. Interstitial Zinc Clusters in Zinc Oxide. *Phys. Rev. B - Condens. Matter Mater. Phys.* **2013**, *88* (24), 1–8.

(38) Momot, A.; Amini, M. N.; Reekmans, G.; Lamoen, D.; Partoens, B.; Slocombe, D. R.; Elen, K.; Adriaensens, P.; Hardy, A.; Van Bael, M. K. A Novel Explanation for the Increased Conductivity in Annealed Al-Doped ZnO: An Insight into Migration of Aluminum and Displacement of Zinc. *Phys. Chem. Chem. Phys.* **2017**, *19*, 27866–27877.

(39) Manjón, F. J.; Marí, B.; Serrano, J.; Romero, A. H. Silent Raman Modes in Zinc Oxide and Related Nitrides. *J. Appl. Phys.* **2005**, *97* (5), 053516.

(40) Sundara Venkatesh, P.; Ramakrishnan, V.; Jeganathan, K. Raman Silent Modes in Vertically Aligned Undoped ZnO Nanorods. *Phys. B Condens. Matter* **2016**, *481*, 204–208.

(41) Decremps, F.; Pellicer-Porres, J.; Saitta, A. M.; Chervin, J. C.; Polian, A. High-Pressure Raman Spectroscopy Study of Wurtzite ZnO. *Phys. Rev. B Condens. Matter Mater. Phys.* **2002**, *65* (9), 921011–921014.

(42) Harriman, T. A.; Bi, Z.; Jia, Q. X.; Lucca, D. A. Frequency Shifts of the E_2^{high} Raman Mode Due to Residual Stress in Epitaxial ZnO Thin Films. *Appl. Phys. Lett.* **2013**, *103* (12), 121904.

(43) Serier, H.; Demourgues, A.; Gaudon, M. Investigation of Ga Substitution in ZnO Powder and Opto-Electronic Properties. *Inorg. Chem.* **2010**, *49* (15), 6853–6858.

TABLE OF CONTENTS GRAPHIC

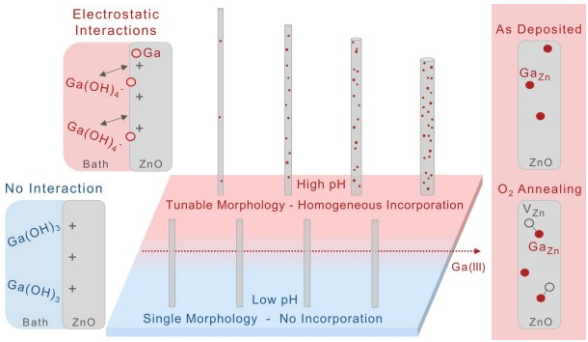

SYNOPSIS

We show a general strategy for the intentional extrinsic doping of ZnO nanowires grown by chemical bath deposition, by investigating in detail the specific case of gallium. Controlling the gallium nitrate concentration and pH in the bath allows a fine tuning of both the morphology and gallium incorporation into ZnO nanowires, emphasizing the electrostatic origin of doping mechanisms in aqueous media. In addition, the post-deposition annealing under oxygen atmosphere modifies the nature of gallium-related defects.